

On Channel Model to Bridge the Gap between MIMO Design and Performance Requirements in 3GPP

Lynda Berrah, Raphael Visoz, Senior Member, IEEE, Didier Le Ruyet, Senior Member, IEEE, Anvar Tukmanov, Senior Member, IEEE, Axel Müller, Member, IEEE, Alexander Hamilton, Member, IEEE, and Matthew Baker, Member, IEEE

Abstract—Accurate channel modeling has become critical for evaluating multiple-input multiple-output (MIMO) performance, especially as 5G standardization matures and efforts toward 6G begin. Recent studies within the 3rd Generation Partnership Project (3GPP) have shown that the tapped delay line (TDL) model, currently used for performance testing, fails to capture the spatial propagation characteristics required for realistic MIMO evaluation. To address this limitation, the reduced clustered delay line (rCDL) model has been introduced as a more accurate alternative with manageable computational complexity, thereby enabling practical implementation in test equipment. This work investigates the rCDL through a comparative analysis with the legacy TDL. First, the angular characteristics of both models are examined. Then, their spatial profiles are compared with real-world measurements from a typical commercial deployment. The results reveal clear deficiencies in the TDL and show that the rCDL better matches measured propagation behavior. As a case study, channel state information (CSI) reporting performance is evaluated in single-user MIMO scenarios. The results show that, with appropriate simulation parameter settings, the rCDL enables clear discrimination between low- and high-resolution CSI reporting schemes, unlike the TDL. These findings confirm the relevance of the rCDL model for MIMO performance evaluation and support its use in current and future standardization efforts.

Index Terms—Spatial channel modeling, rCDL, TDL, MIMO, CSI feedback, 5G/6G performance evaluation, 3GPP.

I. Introduction

WITHIN the 3rd Generation Partnership Project (3GPP), the global standardization body for cellular systems, the responsibility for defining performance requirements for user equipments (UEs) and base stations (BSs) lies primarily with the Radio Access Network Working Group 4 (RAN4). RAN4 evaluates implementations under controlled conditions by specifying channel models, procedures, and test methodologies, thereby ensuring that devices meet the minimum performance targets prescribed

This paper has been submitted to IEEE Transactions on Vehicular Technology for possible publication.

L. Berrah and R. Visoz are with Orange Research, Châtillon, France; L. Berrah is also with CEDRIC, CNAM, Paris, France (e-mail: lynda.berrah@orange.com; raphael.visoz@orange.com).

D. Le Ruyet is with CEDRIC, CNAM, Paris, France (e-mail: didier.leruyet@cnam.fr).

A. Tukmanov is with BT Group Plc, UK (e-mail: anvar.tukmanov@bt.com).

A. Müller is with Nokia Networks, France (e-mail: axel.mueller@nokia.com).

A. Hamilton and M. Baker are with Nokia UK Limited (e-mail: alexander.hamilton@nokia.com; matthew.baker@nokia.com).

in the standard. To this end, RAN4 uses the Tapped Delay Line (TDL) channel model to define performance requirements due to its simplicity and low computational complexity.

In parallel, Radio Access Network Working Group 1 (RAN1), which is responsible for defining physical-layer techniques, conducts complex system-level evaluations that use the fast-fading Spatial Channel Model (SCM) defined in TR 38.901 [1]. RAN1 also resorts to link-level evaluations for specific topics, where the associated channel model is derived from the SCM and is known as the Clustered Delay Line (CDL) model. Both RAN1 system-level and link-level models exhibit the “spatiality” property; that is, they expose multiple, distinct angles of departure and arrival that remain stationary over the fast-fading time scale.

With the increasing sophistication of the multiple-input multiple-output (MIMO) techniques developed in RAN1, notably advanced high-resolution codebooks for channel state information (CSI) reporting [2], [3], the RAN4 TDL channel model becomes unable to yield meaningful performance requirements. To address this limitation, 3GPP RAN4 recently initiated a Study Item (SI) [4] aimed at bridging the gap between RAN1 and RAN4 by adapting the RAN1 CDL channel models to the RAN4 use cases; that is, the resulting RAN4 channel model must preserve the “spatiality” property while maintaining low computational complexity and fast convergence to ease implementation in test equipments.

A. Literature review

MIMO channel models can be classified into analytical and physical models [5]. Analytical models characterize the channel for each transmit-receive antenna link in a mathematical way without explicitly accounting for wave propagation. Moreover, the channel is defined at the antenna port level i.e., the antenna radiation pattern is directly included into the channel and is assumed omnidirectional. As an example, the 3GPP TDL model specified in TS 38.101-4 [6] defines a statistical power-delay profile (PDP) or a list of taps with delays and associated powers. Then, each tap coefficient is generated from a Rayleigh-Jakes distribution [7]. Extensions that incorporate antenna correlation based on the Kronecker model provided a rudimentary means to emulate MIMO behavior, but still lack spatial meaning [8].

In contrast, physical models explicitly characterize the interaction of the antenna pattern with the multipath propagation between the transmit and receive arrays, enabling a more accurate reproduction of radio propagation at the cost of higher computational complexity. They include ray-tracing methods [9], which rely on detailed environmental descriptions and extensive simulations, as well as geometry-based stochastic models. The latter class retains the geometric interpretation of ray-tracing but replaces explicit scatterer positioning with stochastic descriptions based on probability distributions. The COST 273 model [10] is the first model developed within this category that targets MIMO systems. It is based on the empirical observation that scatterers tend to form clusters with similar delays and angular characteristics, thereby introducing the concept of scatterer clusters. Later, COST 2100 [11], generalized this framework to support large-scale MIMO, multi-user scenarios, and time-varying environments. Building on COST actions, 3GPP standardized the SCM [12] for 3G systems, followed by the wideband extended SCM (SCME) [13] for beyond-3G. These models define large-scale parameters (e.g., delay and angular spreads) and small-scale parameters (e.g., per-cluster power, delay, directions of departure and arrival (DoDs/DOAs)) using tabulated probability distributions derived from measurement campaigns [14]. Subsequently, the WINNER and WINNER II models [15], [16] were introduced, covering a broader frequency range, more deployment scenarios, and offering an improved elevation domain modeling. Alongside WINNER II, a reduced-complexity alternative, namely the CDL model, was developed for link-level simulations to facilitate performance comparison and model calibration [16]. The CDL fixes both large- and small-scale parameters to the expected values of the generic model. For 5G and beyond, 3GPP TR 38.901 further extends the WINNER II framework by defining a fast-fading SCM together with its corresponding CDL counterpart [1]. Recently, the aforementioned RAN4 SI on SCM for performance requirements has yielded the reduced CDL (rCDL), defined in TR 38.753 [17]. A corresponding Work Item (WI) has now been approved [18], marking the potential for standardization.

B. Contributions

Throughout the paper, we highlight the limitations of the TDL model, particularly its lack of “spatiality” and demonstrate that the rCDL model, when properly parameterized, represents a promising and accurate alternative for evaluating MIMO performance. To the best of our knowledge, this channel model has not yet been addressed in the literature. Our main contributions are summarized below.

- 1) We first provide a comprehensive overview of the 3GPP TDL and CDL channel models used for link-level simulations, as defined in TR 38.901 [1]. We then derive the rCDL from the legacy RAN1 CDL formulation and provide practical guidelines for its implementation.
- 2) We present Bartlett style DoAs analysis of both the TDL and CDL models. This analysis aims to demonstrate that the CDL provides an accurate basis for MIMO performance evaluation, whereas the spatially agnostic TDL model does not.
- 3) We conducted channel measurements in a commercial MIMO deployment, from which we extracted channel eigenmodes. The results show that the TDL model fails to capture real-world propagation characteristics, while the CDL model matches the measured behavior.
- 4) We provide a detailed overview of the 3GPP Type-I (low-resolution) and enhanced Type-II (high-resolution) codebooks for CSI reporting, emphasizing their underlying design principles. We also describe a practical precoder selection strategy based on these codebooks, along with a physical-layer abstraction framework for link-level performance evaluation.
- 5) Using the proposed framework, we present spectral efficiency results under both TDL and rCDL models, showing that the rCDL could enable clear discrimination between low- and high-resolution codebooks when properly parameterized. We further identify critical parameters that influence the level of discrimination.

C. Paper Organization

The remainder of the paper is organized as follows. Sec. II reviews the TDL model and examines its spatial properties. Sec. III provides background on the CDL model, analyzes its spatial profile, and derives the rCDL variant. Sec. IV presents field measurements conducted in a commercial MIMO deployment. Sec. V discusses CSI reporting based on 3GPP codebooks as an application of MIMO performance evaluation under TDL and rCDL models. Sec. VI concludes the paper.

II. Tapped Delay Line (TDL) Model

A. Description of the TDL Channel Model

Consider a single-input single-output (SISO) non-line-of-sight (NLOS) channel, the passband transmit signal is

$$e(t) = \Re\{x(t) e^{j2\pi f_c t}\}, \quad (1)$$

where $x(t)$ is the baseband transmit signal, f_c is the carrier frequency, and $\Re\{\cdot\}$ denotes the real part. Assuming a finite bandwidth, i.e., discrete propagation delays, the passband received signal can be modeled as a superposition of multipath components (MPCs), that is

$$r_{pb}(t) = \sum_{n=1}^N \sum_{m=1}^M \alpha_{n,m} \Re\left\{ e^{j\phi_{n,m}} x(t - \tau_{n,m}(t)) e^{j2\pi f_c (t - \tau_{n,m}(t))} \right\}, \quad (2)$$

with MPC delays $\tau_{n,m}(t) \in [\tau_n(t) - \Delta\tau, \tau_n(t) + \Delta\tau]$, where $\Delta\tau$ is small enough so that $x(t - \tau_{n,m}(t)) \approx x(t - \tau_n(t))$. We also assume that the delay variation does not significantly

distort the transmit signal, i.e. $x(t - \tau_n(t)) \approx x(t - \tau_n)$, which is true when $\frac{v\Delta f}{c} \ll 1$, where v is the speed, c is the speed of light, and Δf is the transmit signal bandwidth. Under these assumptions, the baseband received signal is

$$r_{bb}(t) = \sum_{n=1}^N \sum_{m=1}^M \alpha_{n,m} e^{j\phi_{n,m}} e^{-j2\pi f_c \tau_{n,m}(t)} x(t - \tau_n). \quad (3)$$

Equivalently, (3) can be written as a linear time-varying convolution as follows

$$r_{bb}(t) = h(t, u) * x(u) \Big|_{u=t}, \quad (4)$$

with the channel impulse response (CIR) given by

$$h(t, \tau) = \sum_{n=1}^N c_n(t) \delta(\tau - \tau_n), \quad (5)$$

where $\delta(\cdot)$ is the Dirac delta function and the complex gain associated with tap n is written as

$$c_n(t) = \sum_{m=1}^M \alpha_{n,m} e^{j\phi_{n,m}} e^{-j2\pi f_c \tau_{n,m}(t)}. \quad (6)$$

The channel is described by N taps, each being the superposition of M MPCs arriving with nearly the same delays. $\alpha_{n,m}$ and $\phi_{n,m}$ denote the amplitude and initial phase of the m -th ray belonging to tap n , respectively. At a given time t , for large M , by the central limit theorem $c_n(t)$ is well modeled by a complex Gaussian process; consequently, $|c_n(t)|$ is Rayleigh distributed. Empirical measurements in NLOS scenarios support the Rayleigh fading assumption.

In the standard, the TDL model in (5) is specified by the tables in [6, Appendix B], each corresponding to a frequency band and profile (TDL-A/B/C for NLOS and TDL-D for LOS). These tables define the number of taps and their associated delays and powers. Furthermore, the standard specifies that the tap coefficients exhibit Rayleigh fading for NLOS components.

B. Doppler Spectrum

Consider the receiver moving with velocity vector \mathbf{v} , and let $\mathbf{u}_{n,m}$ be the unit vector corresponding to the inverse direction of arrival of the ray m in cluster n , the delay evolves as

$$\tau_{n,m}(t) = \tau_{n,m} - \frac{\mathbf{u}_{n,m} \cdot \mathbf{v}}{c} t. \quad (7)$$

Let $\varphi_{n,m} := (\phi_{n,m} - 2\pi f_c \tau_{n,m}(t))$ and the maximum Doppler shift $f_D := v/\lambda_0$, where v is the speed and λ_0 denotes the wavelength. Assuming two-dimensional scattering, i.e., the angular domains reduce to the azimuthal domain, and let $\theta_{n,m}$ be the angle between $\mathbf{u}_{n,m}$ and \mathbf{v} , the gain for tap n in (6) can be re-written as

$$c_n(t) = \sum_{m=1}^M \alpha_{n,m} e^{j\varphi_{n,m}} e^{j2\pi f_D t \cos(\theta_{n,m})}. \quad (8)$$

This channel time variation is characterized by its power spectral density (PSD), also called the Doppler spectrum. With a large number of MPCs and i.i.d. angles $\theta_{n,m} \sim$

$\mathcal{U}[0, 2\pi)$, the normalized temporal autocorrelation is given as [19]

$$R(\tau) = J_0(2\pi f_D \tau), \quad (9)$$

where $J_0(\cdot)$ is the zero-order Bessel function of the first kind. By taking the Fourier transform of (9), the Doppler spectrum reduces to the so-called Jakes spectrum

$$S(f) = \frac{1}{\pi f_D \sqrt{1 - (f/f_D)^2}}, \quad |f| < f_D. \quad (10)$$

and $S(f) = 0$ for $|f| \geq f_D$. This is also referred to as the Clarke's model. Channel coefficients can be generated by means of a sum-of-sinusoids (SoS) model as defined below.

Definition: Original Clarke's SoS implementation [19]

$$c_n(t) = \frac{1}{\sqrt{M_0}} \sum_{m=1}^{M_0} e^{j(2\pi f_D t \cos(\theta_{n,m}) + \varphi_{n,m})} \quad (11)$$

where M_0 denotes the number of Doppler-shifted sinusoids. Here, $\varphi_{n,m}$ and $\theta_{n,m}$ are statistically independent and uniformly distributed on $[0, 2\pi)$. The value of M_0 must be large enough to approximate Rayleigh statistics.

Based on the SoS model, Jakes derived a simplified simulator in [20] using for tap $n \in \{1, \dots, N\}$

$$\theta_{n,m} = \frac{2\pi m}{M_0} \text{ and } \varphi_{n,m} = 0 \quad \forall m \in \{1, \dots, M_0\}. \quad (12)$$

This deterministic construction makes it difficult to generate multiple uncorrelated fading processes for MIMO systems. Thus, several modified Jakes simulators have been proposed; a commonly used implementation is described in [7].

C. Extension to MIMO Scenarios

The TDL model in (5) extends to MIMO systems by treating each transmit–receive antenna pair as an independent SISO channel, this by replacing scalar taps with matrices as follows

$$\mathbf{H}(t, \tau) = \sum_{n=1}^N \tilde{\mathbf{C}}_n(t) \delta(\tau - \tau_n), \quad (13)$$

where $\tilde{\mathbf{C}}_n(t) \in \mathbb{C}^{N_R \times N_T}$, with N_R and N_T denoting the numbers of receive and transmit antennas, respectively.

Spatial correlation can be imposed on the entries of $\tilde{\mathbf{C}}_n(t)$ to match the desired channel properties. Let $\tilde{\mathbf{c}}_n(t) := \text{vec}(\tilde{\mathbf{C}}_n(t))$, where $\text{vec}(\cdot)$ stacks the $N_R \times N_T$ matrix into a column vector. The coefficients for tap n are generated as

$$\tilde{\mathbf{c}}_n(t) = (\mathbf{R}_n)^{1/2} \mathbf{c}_n(t), \quad (14)$$

where $(\mathbf{R}_n)^{1/2} \in \mathbb{C}^{N_R N_T \times N_R N_T}$ is any square-root decomposition of the spatial correlation matrix \mathbf{R}_n , and $\mathbf{c}_n(t) \in \mathbb{C}^{N_R N_T \times 1}$ has i.i.d. Rayleigh fading coefficients generated via the SoS method at time t .

Correlation matrices are typically derived analytically given an angular power distribution and antenna radiation patterns [8]. In the 3GPP standard [6], spatial correlations are explicitly defined; however, this is achieved by adopting several simplifying assumptions, resulting in a loss of spatial meaning. These assumptions are listed below.

- Kronecker Model: spatial correlations are modeled as the Kronecker product of the correlation matrices defined independently at the transmitter and the receiver [8], [21].
- Fixed Correlation Matrices: Use of 2×2 correlation matrices, assumed identical across all taps for settings with 2 transmit and receive antennas. In realistic propagation environments, this assumption is not valid, as different scatterers typically exhibit distinct spatial profiles [22].
- Absence of Phase Information: Phase is disregarded and only the magnitudes of the correlation matrices are considered. This potentially obscures important spatial information, as in practice multiple power spectra can result in identical magnitude values [23].
- Extension to Higher Dimensions: The model is extended to 4×4 correlation matrices using an ad-hoc exponential decay interpolation [24], and later to 8×8 [25]. However, the justification of this dimensional extension based on the original measurements remains unclear [26].

D. Spatial Profile

We define the receive spatial profile of a channel realization as the receive signal power obtained when discrete Fourier transform (DFT) beams are applied over varying DoAs. This concept readily extends to averaging across multiple channel realizations and transmit directions. This simple approach, referred to as Bartlett analysis [27], is used to estimate the power azimuth spectrum of the channel model. More complex high-resolution methods, such as MUSIC and ESPRIT, also exist; however, Bartlett approach is sufficient to provide insights into the spatial characteristics of the TDL model.

In Fig. 1, we examine the spatial profile of TDL models without antenna correlation (i.e., low correlation in 3GPP parlance). We consider a MIMO system with 8 transmit and receive antenna ports at a carrier frequency $f_c = 3.5$ GHz, with a system bandwidth of 40 MHz, and a sub-carrier spacing of 30 kHz. We adopt a TDL-C profile with a delay spread of 300 ns and a maximum Doppler frequency of 100 Hz, corresponding to a UE speed of 30 Km/h. This configuration is referred to as TDLC300-100 and is defined in [6, Table B.2.1.1-4]. For TDLC300-100 with low correlation, we observe that the large-scale spatial preference of the per-resource element (RE) channels becomes mostly decorrelated after 2.5 ms. Although the speed of change of the spatial profile can be theoretically controlled using the maximum Doppler frequency, it is here misaligned with expectations. Moreover, the large-scale spatial properties are hardly repeatable between

implementations, and expected mid-term stable directions are not present. Following the aggregation of uncorrelated SISO channel coefficients into a MIMO channel model, we also note that realizations of the TDL low model are almost surely full rank. This excessive randomness of the spatial profile (illustrated in Fig. 1) poses challenges for precoding and CSI reporting procedures, which were recognized in 3GPP.

To address this issue, antenna correlations were introduced based on the Kronecker model for CSI performance requirements definition. However, the chosen antenna correlation models introduce a highly exaggerated spatial directivity towards the broadsight direction in all channel realizations, REs, and paths, which does not change over time. This behavior is illustrated in Fig. 2 for TDLC300-100 with medium correlation (spatial correlation matrix medium-A defined in [6, Sec. B.2.3.1.2]). From this observation, it also follows that TDL channel realizations employing such antenna correlation are highly rank deficient; increasing the antenna number above 3 does not improve spatial diversity due to exceedingly small antenna correlation coefficients. Additionally, both signal and interference are consistently received from the broadsight direction, independently of the chosen precoder.

III. Clustered Delay Line (CDL) Model

The CDL model represents the propagation channel as a superposition of multiple distinct clusters, each corresponding to a dominant scattering region characterized by a specific propagation delay, average power, and mean angles of departure and arrival. Within each cluster, several rays or MPCs share the same delay but exhibit small variations in their angles, which are distributed around the cluster mean according to predefined angular spreads [14]. Fig. 3 illustrates a cluster composed of multiple scatterers, modeled as first- and last-bounce ellipsoids, as observed from the BS and UE.

The CDL model is defined by fixed large- and small-scale parameters (LSPs and SSPs, respectively). The

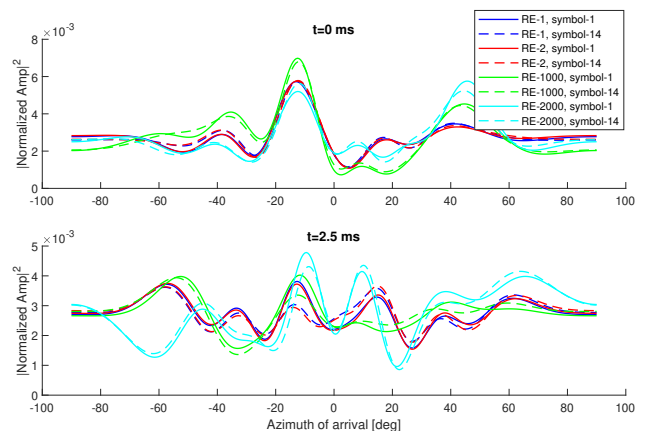


Fig. 1. Bartlett DoA analysis comparing RE-wise temporal evolution of the TDLC300-100 model with low antenna correlation; high spatial randomness and rapid per-RE angular decorrelation are observed.

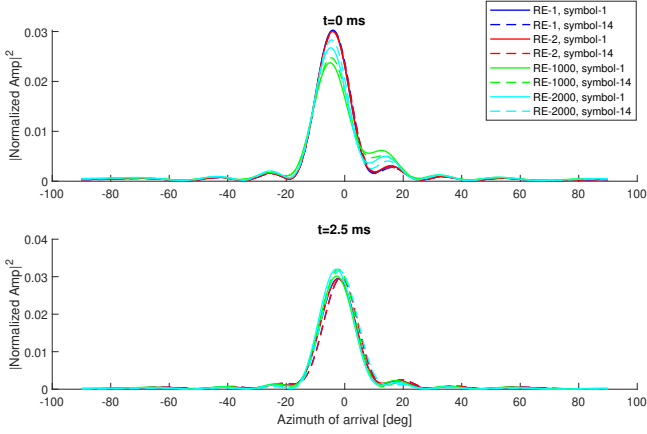


Fig. 2. Bartlett DoA analysis comparing RE-wise temporal evolution of the TDLC300-100 model with medium-A antenna correlation; a single DoA, constant across time and REs, is observed.

LSPs include the delay spread and angular spreads, while the SSPs comprise cluster power, delay, DoAs/DoDs, cross-polarization power ratio (XPR), and the per-cluster angular spreads in both azimuth and zenith, as illustrated in Fig. 3. These per-cluster parameters are set to median values derived from the generic stochastic fast-fading SCM model, which defines statistical distributions for LSPs and SSPs [1, Sec. 7.5], based on measurement campaigns in various environments (e.g., Urban Macro (UMa), Indoor Factory (InF)). The CDL model is fully specified through tables in [1, Sec. 7.7] for different profiles: CDL-A/B/C for NLOS and CDL-D/E for LOS scenarios.

A. Description of the CDL Channel Model

The model considers N clusters, each comprising M rays. The channel coefficient in NLOS scenario for transmit antenna s , receive antenna u , and cluster n at time t

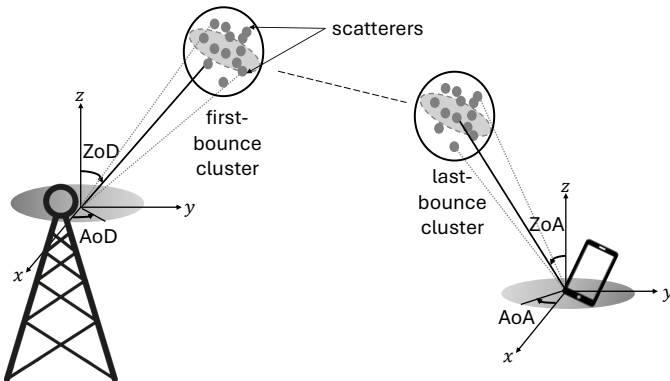


Fig. 3. Illustration of the CDL model. The cluster is depicted as an ellipsoid that groups scatterers, and has a mean azimuth/zenith of departure/arrival, denoted AoD, ZoD, AoA, and ZoA, respectively.

is

$$H_{u,s,n}(t) = \sqrt{\frac{P_n}{M}} \sum_{m=1}^M \mathbf{F}_{rx,u}(\theta_{n,m,ZoA}, \phi_{n,m,AoA})^T \mathbf{M}_{pol} \mathbf{F}_{tx,s}(\theta_{n,m,ZoD}, \phi_{n,m,AoD}) \exp\left(\frac{j2\pi}{\lambda_0} \hat{\mathbf{r}}_{rx,n,m}^T \bar{\mathbf{d}}_{rx,u}\right) \exp\left(\frac{j2\pi}{\lambda_0} \hat{\mathbf{r}}_{tx,n,m}^T \bar{\mathbf{d}}_{tx,s}\right) \exp\left(\frac{j2\pi}{\lambda_0} \hat{\mathbf{r}}_{rx,n,m}^T \bar{\mathbf{v}} t\right). \quad (15)$$

Eq. (15) is expressed in spherical coordinates, where θ and ϕ denote the zenith (ZoD, ZoA) and azimuth (AoD, AoA) angles of departure and arrival, respectively (with $\theta = 90^\circ$ pointing toward the horizon). P_n represents the power of the n -th cluster. For clarity, we omit indices in the following description. The vectors \mathbf{F}_{tx} and \mathbf{F}_{rx} correspond to the transmit and receive antenna field patterns, respectively, while \mathbf{M}_{pol} denotes the polarization coupling matrix. The unit vectors $\hat{\mathbf{r}}_{tx}$ and $\hat{\mathbf{r}}_{rx}$ define the directions of propagation from the transmitter and toward the receiver, and the vectors $\bar{\mathbf{d}}_{tx}$ and $\bar{\mathbf{d}}_{rx}$ specify the positions of the transmit and receive antenna elements relative to the center of the panels. Finally, $\bar{\mathbf{v}}$ represents the UE velocity vector. In the following, we provide a detailed description of each term in (15).

1. Angle definition: The AoD of ray m in cluster n is

$$\phi_{n,m,AoD} = \phi_{n,AoD} + c_{ASD}\alpha_m, \quad (16)$$

where $\phi_{n,AoD}$ is the cluster mean AoD and c_{ASD} is the per-cluster azimuth spread of departure (ASD), both tabulated in [1], e.g., Table 7.7.1-3 for CDL-C. The ray offset angles α_m are also fixed by 3GPP [1, Table 7.5-3]. Other angles (i.e. AoA, ZoD, and ZoA) are defined analogously using their respective cluster means and per-cluster spreads. Within each cluster, the previously defined angles are then randomly coupled to form the final ray directions.

2. Antenna Modeling: The field pattern describes the spatial distribution of the radiated electromagnetic field from a given antenna element. In polar coordinates, it is given as

$$\mathbf{F}''(\theta'', \phi'') = \begin{bmatrix} F''_{\theta''}(\theta'', \phi'') \\ F''_{\phi''}(\theta'', \phi'') \end{bmatrix}, \quad (17)$$

where $F''_{\theta''}$ and $F''_{\phi''}$ denote the co-polar and cross-polar components of the field in the directions of the spherical unit vectors $\hat{\theta}$ and $\hat{\phi}$, respectively. The corresponding power radiation pattern is given as

$$A''(\theta, \phi) = |F''_{\theta''}(\theta'', \phi'')|^2 + |F''_{\phi''}(\theta'', \phi'')|^2. \quad (18)$$

For a single purely vertically polarized antenna located at the origin of the coordinate system, the field pattern simplifies to

$$\mathbf{F}''(\theta'', \phi'') = \begin{bmatrix} \sqrt{A''(\theta'', \phi'')} \\ 0 \end{bmatrix}, \quad (19)$$

with $A''(\theta'', \phi'') = 0$ dBi for an isotropic radiator, and defined according to formula in [1, Table 7.3-1] for a sector antenna.

To generalize the definition to arbitrary antenna orientations, we introduce a hierarchy of coordinate systems. A global coordinate system (GCS) provides a common reference for the transmitter and receiver, in which all the terms in (15) are expressed in the standard. The local coordinate systems (LCS') are obtained by rotating the GCS according to the orientation of each antenna panel, described by the angles (α, β, γ) . Here, α is the bearing angle (rotation about the z -axis), β is the downtilt angle (rotation about the y -axis), and γ is the slant angle (rotation about the x -axis). Separate LCS' are defined for the BS and UE panels. To account for polarization slant, we introduce double-primed local coordinate systems (LCS''). Each LCS'' is obtained by rotating the corresponding LCS' about the x -axis by the polarization slant angle ζ , assuming the antenna panel lies in the (y', z') plane. Hence, for each polarization of each panel (BS and UE), we define a separate LCS'', resulting in four double-primed coordinate systems. Within each LCS'', the antenna elements of the considered polarization are treated as vertically polarized, so that the formula in (17) applies. The GCS-to-LCS transformations are detailed in the Appendix.

3. Polarization Coupling: The polarization matrix \mathbf{M}_{pol} describes how the polarization changes on the propagation path from the transmitter to the receiver. It is modeled based on random coefficients as

$$\mathbf{M}_{pol} = \begin{bmatrix} \exp(j\Phi_{n,m}^{\theta\theta}) & \frac{1}{\sqrt{\kappa_{n,m}}} \exp(j\Phi_{n,m}^{\theta\phi}) \\ \frac{1}{\sqrt{\kappa_{n,m}}} \exp(j\Phi_{n,m}^{\phi\theta}) & \exp(j\Phi_{n,m}^{\phi\phi}) \end{bmatrix} \quad (20)$$

Here, the phases for the four polarization combinations $\{\Phi_{n,m}^{\theta\theta}, \Phi_{n,m}^{\theta\phi}, \Phi_{n,m}^{\phi\theta}, \Phi_{n,m}^{\phi\phi}\}$ are drawn from a uniform distribution on $[-\pi, \pi)$. The coefficient $\kappa_{n,m}$ is the XPR for ray m in cluster n , it quantifies the separation between the two polarized channels due to different orientations. CDL models use a fixed XPR for all clusters and rays, tabulated in [1, Table 7.7.1-3] for CDL-C.

4. Phase Shifts across Antenna Arrays: Here, we express the phase shift associated with the scatterer m in cluster n when considering transmit antenna element s and receive antenna element u , relative to a hypothetical ray assuming that the antenna elements are located at the centers of the transmit and receive panels. Assuming that the distance between the scatterer and the array is much larger than the array aperture, the wave arriving at or departing from any scatterer can be approximated as a plane wave. Under this far-field approximation, the phase shift for the transmit antenna–scatterer link is

$$\Delta\varphi_{tx,s,n,m} = \exp\left(\frac{j2\pi}{\lambda_0} \hat{\mathbf{r}}_{tx,n,m}^T \cdot \bar{\mathbf{d}}_{tx,s}\right), \quad (21)$$

and for the scatterer–receive antenna link as

$$\Delta\varphi_{rx,u,n,m} = \exp\left(\frac{j2\pi}{\lambda_0} \hat{\mathbf{r}}_{rx,n,m}^T \cdot \bar{\mathbf{d}}_{rx,u}\right). \quad (22)$$

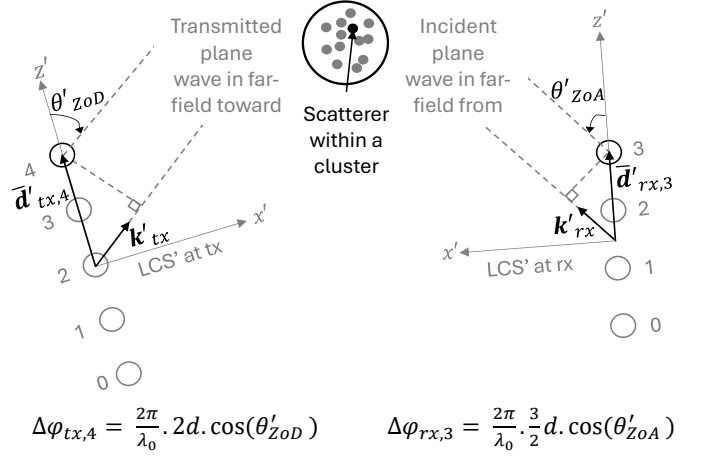


Fig. 4. Phase shifts for a given ray within a scatterer cluster for a given transmit and receive uniform linear arrays (ULA), illustrating the effect of antenna element positions on the received signal phase.

The wave vector for the link between transmit antenna s and scatterer m within cluster n is expressed as

$$\mathbf{k}_{tx,n,m} = \frac{2\pi}{\lambda_0} \hat{\mathbf{r}}_{tx,n,m} = \frac{2\pi}{\lambda_0} \begin{bmatrix} \sin \theta_{n,m,ZoD} \cos \phi_{n,m,AoD} \\ \sin \theta_{n,m,ZoD} \sin \phi_{n,m,AoD} \\ \cos \theta_{n,m,ZoD} \end{bmatrix}, \quad (23)$$

and the location vector of the transmit antenna s , expressed in the BS LCS' as

$$\bar{\mathbf{d}}'_{tx,s} = [0 \quad n_s d_y - y_c \quad m_s d_z - z_c]^T, \quad (24)$$

where (d_y, d_z) denote the inter-element spacings along the horizontal and vertical dimensions, respectively, and (n_s, m_s) denote the antenna element indices. The origin of the GCS and LCS' is assumed to be located at the center of the antenna panel. Accordingly, in (24), $(y_c, z_c) := (\frac{N_y-1}{2}d_y, \frac{N_z-1}{2}d_z)$ represent the coordinates of the panel center, where N_y and N_z denote the number of antenna elements along the y - and z -axes, respectively. However, the absolute choice of the GCS origin for the CDL model is inconsequential, since the phase term depends only on the relative orientation between the wave propagation direction and the antenna element displacement vector, provided both are expressed in the same coordinate system. Consequently, the scalar product between (23) and (24) can be evaluated directly in the LCS'. To this end, the wave propagation vector is transformed to LCS' according to

$$\hat{\mathbf{r}}'_{tx,n,m} = \mathbf{R}^T \hat{\mathbf{r}}_{tx,n,m}, \quad (25)$$

where the rotation matrix \mathbf{R} is detailed in the Appendix. The phase shifts at the receiver are computed analogously by considering the arrival angles in (23) and the antenna locations on the receive panel in (24). Fig. 4 illustrates the phase shifts in a two-dimensional propagation scenario.

5. Doppler Effect: The temporal evolution of the CIR is modeled based on a Doppler shift that depends on the

velocity v , the user direction of motion (ϕ_v, θ_v) , and the arrival angles as in Sec. II-B. It is given as

$$\frac{\hat{\mathbf{r}}_{rx,n,m}^T \bar{\mathbf{v}}}{\lambda_0}, \text{ with } \bar{\mathbf{v}} = v [\sin \theta_v \cos \phi_v \quad \sin \theta_v \sin \phi_v \quad \cos \theta_v]^T. \quad (26)$$

6. Antenna Numbering: The channel coefficients calculated based on (15) are stacked from bottom to top, column by column, as described in [28] starting by the co-polarized then the cross-polarized elements. This is important as the precoder structure as defined by 3GPP assumes this numbering.

B. Spatial Profile

A Bartlett-style spatial profile analysis, identical to that described in Sec. II-D, is applied to the CDL model. We consider the CDL-C profile (UMa scenario) with a delay spread of 365 ns and a maximum Doppler shift of 100 Hz in order to obtain results that are comparable with those of the TDL model. The same carrier frequency and bandwidth are used for both models. Unlike the TDL model, which defines the channel directly at the antenna port level, here we consider 128 transmit antenna elements mapped to 8 antenna ports as described in [29], and 8 receive antenna ports.

The resulting spatial profile in Fig. 5 demonstrates that the CDL model captures the spatial characteristics of practical MIMO deployments, i.e. the presence of multiple mid-term stable DoAs. An additional advantage of the CDL model is that the channel rank naturally follows from the antenna modeling and cluster configuration. Consequently, the rank is inherent to the propagation and antenna assumptions, rather than being imposed through external antenna correlation models.

C. Derivation of the Reduced CDL Model

The rCDL model has been defined within RAN4 for the performance evaluation of MIMO features. Its objective is to preserve the spatial characteristics of the RAN1 CDL while enabling fast convergence and reduced

computational complexity to facilitate implementation in test equipment. Specified in 3GPP TR 38.753 [17] as rCDL-C, it is derived from the CDL-C UMa profile through three key modifications. First, angular spreads are updated using a defined procedure with explicitly specified target values. Second, model randomness is reduced using the framework in 3GPP TR 38.827 [29], enabling fast convergence and cross-simulator alignment. In addition, antenna array virtualization is explicitly specified to allow consistent comparisons. Finally, the number of clusters is reduced to lower complexity.

1. Angular Scaling Procedure: The angles of departure and arrival of the RAN1 CDL-C (or CDL-C 901) are scaled to achieve desired angular spreads as

$$\varphi_{n,scaled} = \text{wrap}\left(\frac{AS_{desired}}{AS} \cdot \text{wrap}(\varphi_n - \mu_\varphi) + \mu_\varphi\right). \quad (27)$$

Per-cluster spreads are scaled as $c_{scaled} = (AS_{desired}/AS)c$. Then, the angles of arrival/departure for rays are obtained as

$$\varphi_{n,m,scaled} = \varphi_{n,scaled} + c_{scaled} \alpha_m. \quad (28)$$

Here, AS and μ_φ denote the angular spreads and the power weighted mean angles of the CDL-C 901 model, calculated based on the formulas provided in [1, Annex A]. Also, c denotes the per-cluster spreads of arrival and departure angles given in [1, Table 7.7.1-3], and α_m represents the offset angle for ray m specified in [1, Table 7.5-3]. Finally, we define

$$\text{wrap}(x) = (x + 180) \bmod 360 - 180 \quad (29)$$

The desired spreads $AS_{desired}$ are provided in [17, Table Table 5.1.3.1-1]¹. The parameters of the rCDL-C provided in [17, Table 5.1.3.3.1-1], account for the desired angular spreads.

2. Randomness Reduction Framework: The randomness reduction framework employs a fixed coupling pattern for ray angles within a given cluster, the couplings are provided in [17, Table 5.1.3.2-1]. It also uses fixed phases for the polarization coupling matrix defined in (20), the values are provided in [17, Table 5.1.3.2-2].

3. Antenna Array Virtualization: The antenna panel consists of single- or dual-polarized radiating elements arranged on a two-dimensional grid defined by rows and columns. The panel can be partitioned into subarrays, where each subarray comprises a set of co-polarized elements that are mapped to a single antenna port through an antenna array virtualizer (AAV). Unless a steering direction is specified, broadside emission is assumed; accordingly, equal real-valued weights are applied when combining the channel coefficients of the antenna elements (in (15)) within each subarray.

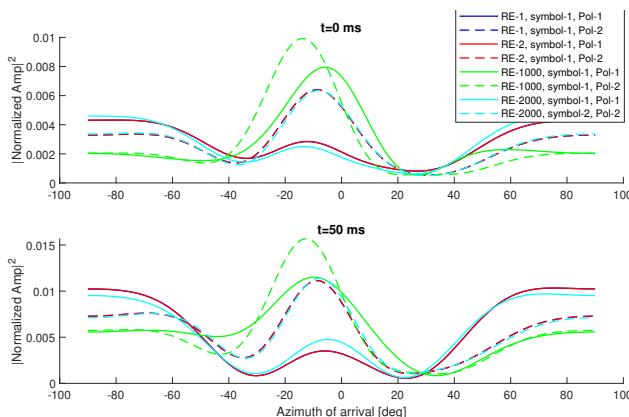


Fig. 5. Bartlett DoA analysis comparing RE-wise temporal evolution of the CDL-C UMa model with 365 ns delay spread and 100 Hz Doppler frequency; multiple mid-term stable DoAs are observed.

¹The method described here corresponds to TR 38.753 V19.0.0; however, the scaling procedure and desired spreads are still under discussion.

4. Cluster Reduction: The number of clusters is reduced from $N = 24$ for RAN1 CDL-C to $N' = 12$, which reduces the complexity and facilitates real-time generation in the simulators used for performance testing. This truncation retains the N' clusters with the highest power after accounting for the antenna field patterns and the AAV. To maintain the desired spread, delay rescaling is applied as follows

$$\tau_{n,scaled} = \frac{DS_{desired}}{DS_{truncated}} \tau_n, \quad (30)$$

where the rms delay spread after truncation is calculated as

$$DS_{truncated} = \sqrt{\frac{\sum_{n=1}^{N'} P_n \tau_n^2}{\sum_{n=1}^{N'} P_n} - \left(\frac{\sum_{n=1}^{N'} P_n \tau_n}{\sum_{n=1}^{N'} P_n} \right)^2}, \quad (31)$$

where τ_n and P_n denote the delay and power of the n -th RAN1 CDL-C cluster, respectively. The delays listed in [17, Table 5.1.3.3.1-1] already account for the rescaling described above with $DS_{desired} = 365$ ns. Angular scaling is not re-applied to enforce the target values; consequently, the removal of low-power clusters may introduce small deviations. The truncation procedure is detailed in [17, Annex B.3]. Detailed implementation guidelines for generating the rCDL-C channel are provided in Algorithm 1.

D. Extension to multi-user MIMO

To evaluate multi-user (MU) effect related performance impacts, single and multi-cell MU channel model extensions are required. To correctly model interference effects and their mitigation, the MU channel model needs to be spatially consistent, i.e., the large-scale environment should stay consistent for different positions of users, or at

Algorithm 1 channel generation procedure for the rCDL

- 1: Set antenna array parameters (define panel structure and orientation) and network layout (speed and direction of motion of UE, carrier frequency, and bandwidth).
 - 2: Set angular and delay spreads according to the scenario.
 - 3: Operate angular and/or delay scaling as described in III-C-1 and III-C-4, respectively.
 - 4: Define sub-path angles based on Eq. (28).
 - 5: Couple angles within clusters using [17, Table 5.1.3.2-1].
 - 6: Calculate the field patterns in the GCS as described in III-A-2, by operating transformations in the Appendix.
 - 7: Define the polarization matrices by using fixed phases defined in [17, Table 5.1.3.2-2].
 - 8: Calculate the phase shifts as in III-A-4.
 - 9: Calculate the Doppler term as in III-A-5.
 - 10: Apply AAV, if defined, as described in III-C-3.
-

least the spatial properties shall consistently correlate with the positions of users and transmitters. The CDL model discussed in this paper can be readily extended to MU setups, by employing the spatial consistency procedures described in [1, Sec. 7.6.3]. Channel model parameter tables for additional spatially correlated users can be created using the procedure to move the initial user to another position, which may be close by to share common large-scale environmental features, or far away to decorrelate.

IV. Field Measurements

Sections II and III introduced the TDL and CDL channel models and discussed their respective benefits and drawbacks. This section assesses how well these model classes capture the MIMO channel properties that govern spatial multiplexing in operational networks. Since multiplexing capability is commonly characterized by channel singular values or post-equalization SINR [30], we compare post-equalization SINR derived from measured MIMO channels with SINR profiles from CDL and TDL model realizations. For further details on angular spreads and multipath arrival characteristics, see [31].

A. Measurement conditions

Channel matrices \mathbf{H} were measured using a setup described in [32, Sec. 2]. The setup utilizes cell-specific reference signals (CRS) transmitted in a 15 MHz downlink channel at 2162.2 MHz center frequency from a typical commercial base station in a campus-type environment in Martlesham Heath, England. The base station and the receiving equipment included 4 transmitting and 4 receiving ports, respectively. Measurements were conducted in static positions during office hours, with some movement of people and vehicles in the coverage sector, yet not in the vicinity of the measurement setup.

B. Main observations

Assuming full CSI knowledge, singular value decomposition (SVD) precoding is applied at the transmitter, and the corresponding SVD combining at the receiver for each channel realization \mathbf{H} . This allows the typical impact of the underlying spatial MIMO propagation environment on multiplexing capability to be made explicit. The histograms in Fig. 6 indicate a spread of approximately 28 dB between the strongest and weakest eigenmodes of the 4-by-4 MIMO channel realizations. Although the magnitude of the spread varies with the environment and transmission strategy, the presence of a spread is typical to practical MIMO channels.

Post-equalization SINR distributions for realizations of the TDL and CDL models are provided in Fig. 7 and Fig. 8, respectively, assuming a linear minimum mean square (LMMSE) receiver. Figures consider an 8-by-8 MIMO system and precoding based on 3GPP Type-I codebook. Detailed precoder description and SINR formulas are provided in Sec. V. Since TDL channels lack

”spatiality” property, any eigenmode is as good as any other, resulting in identical overlapping distributions of SINR per spatial layer in Fig. 7. In contrast, in Fig. 8, the SINR for the same transmission strategy applied to a CDL channel does demonstrate a spread in eigenmodes comparable to observations from deployment.

Designing a transmission strategy that exploits the practically observed eigenmode spread is nontrivial, as it entails, for example, selecting the number of spatial layers to activate as shown in Sec. V-C, as well as determining the power allocation across the active layers. Consequently, both the development of transmission schemes and the specification of meaningful performance requirements for MIMO systems should be carried out using models that are capable of capturing this overall eigenmode-spread effect.

V. Application to CSI Feedback based on Low- and High-Resolution Codebooks

3GPP adopts a limited CSI feedback framework in which the UE measures the downlink channel based on CSI

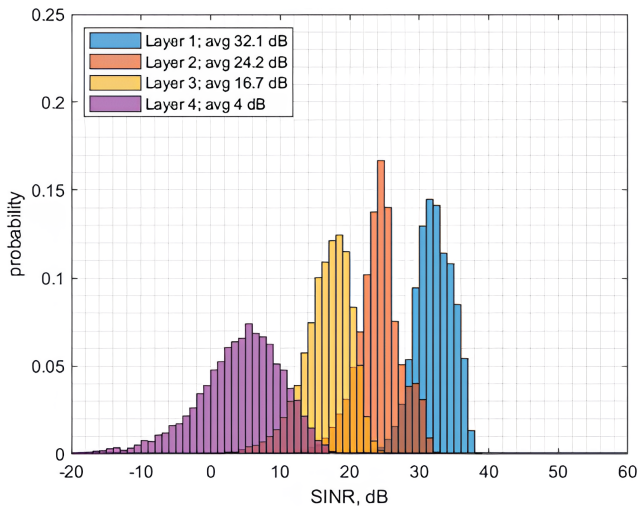


Fig. 6. Histograms of per-layer SINR assuming SVD precoding and combining based on measured MIMO channels.

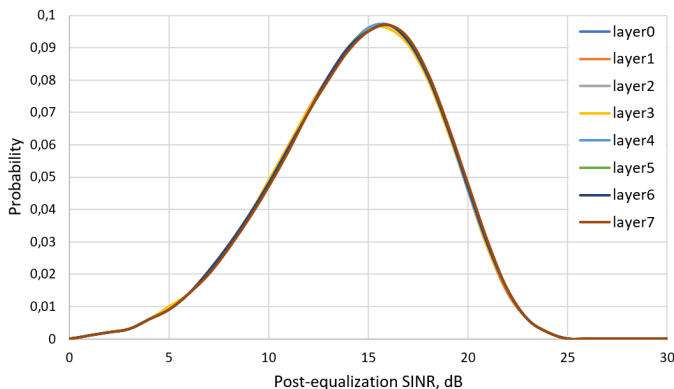


Fig. 7. Simulated post-equalization SINR profile for an 8×8 MIMO system under the TDLC300 channel model, using a randomly selected precoder from Type-I codebook and an LMMSE receiver.

reference signals (CSI-RS), then feeds back a CSI report to the BS. The CSI report includes a rank indicator (RI), a channel quality indicator (CQI), and a precoding matrix indicator (PMI) selected from a standardized codebook [3]. In this section, we evaluate low- and high-resolution PMI reporting using the Release 15 Type-I and Release 16 enhanced Type-II (eType-II) codebooks under legacy TDL and rCDL channel models as a case study for MIMO performance evaluation.

A. 3GPP Downlink MIMO Codebooks

To balance the trade-off between CSI resolution and feedback overhead, 3GPP employs precoder compression based on inverse DFT (IDFT) bases. We define the spatial domain (SD) compression applicable to all 3GPP codebooks specified for 5G New Radio (NR). Consider a two-dimensional planar transmit array with N_1 and N_2 antenna ports in the horizontal and vertical dimensions, respectively. SD compression selects oversampled 2D-IDFT vectors from a grid, where each vector points to a specific region (oversampling improves angular accuracy). The vectors are defined by the Kronecker product

$$\mathbf{u}_{n_1, n_2}(q_1, q_2) = \mathbf{u}'_{n_1}(q_1) \otimes \mathbf{u}''_{n_2}(q_2) \in \mathbb{C}^{N_1 N_2}, \quad (32a)$$

where the horizontal and vertical IDFT vectors are defined as

$$\mathbf{u}'_{n_1}(q_1) = \left[1 \ e^{j \frac{2\pi n_1}{N_1}} \ \dots \ e^{j \frac{2\pi n_1 (N_1 - 1)}{N_1}} \right]^T \odot \mathbf{v}_1(q_1), \quad (32b)$$

$$\mathbf{u}''_{n_2}(q_2) = \left[1 \ e^{j \frac{2\pi n_2}{N_2}} \ \dots \ e^{j \frac{2\pi n_2 (N_2 - 1)}{N_2}} \right]^T \odot \mathbf{v}_2(q_2), \quad (32c)$$

where \odot denotes the Hadamard product, and the rotation vector is

$$\mathbf{v}_i(q_i) = \left[\left(e^{j \frac{2\pi q_i}{O_i N_i}} \right)^0 \ \dots \ \left(e^{j \frac{2\pi q_i}{O_i N_i}} \right)^{N_i - 1} \right]^T, \text{ for } i = 1, 2. \quad (32d)$$

Here, $n_1 \in \{0, \dots, N_1 - 1\}$, $n_2 \in \{0, \dots, N_2 - 1\}$, $q_1 \in \{0, \dots, O_1 - 1\}$, and $q_2 \in \{0, \dots, O_2 - 1\}$, where O_1 and O_2 denote the horizontal and vertical oversampling factors, respectively [33]. This construction defines a grid

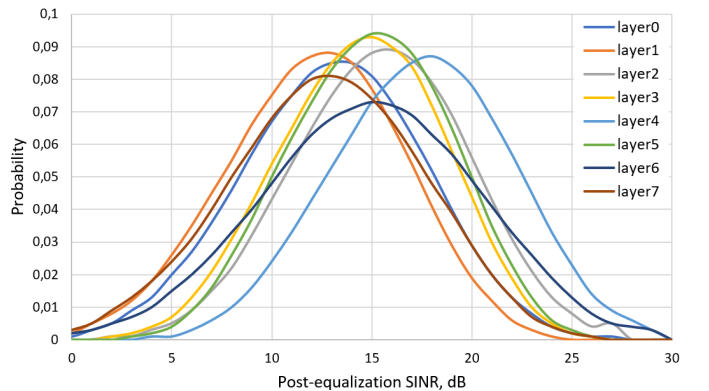


Fig. 8. Simulated post-equalization SINR profile for an 8×8 MIMO system under the CDL-C channel model with 365 ns delay spread, using a randomly selected precoder from Type-I codebook and an LMMSE receiver.

\mathcal{G} of $N_1 O_1 \times N_2 O_2$ beams from which the dominant directions are selected for SD compression.

1. Type-I Codebook: For rank 1, the precoder is given by

$$\mathbf{w} = \frac{1}{\sqrt{2N_1 N_2}} \begin{bmatrix} \mathbf{u}_{n_1, n_2}(q_1, q_2) \\ \varphi \mathbf{u}_{n_1, n_2}(q_1, q_2) \end{bmatrix} \in \mathbb{C}^{2N_1 N_2}, \quad (33)$$

where the dominant beam is selected from the grid \mathcal{G} , and the co-phasing between polarizations φ is chosen from the set $\{1, j, -1, -j\}$. The precoder can equivalently be expressed as the product of an SD compression (beam) matrix $\mathbf{W}_1 \in \mathbb{C}^{2N_1 N_2 \times 2}$ and a co-phasing vector $\mathbf{w}_2 \in \mathbb{C}^2$, that is

$$\mathbf{w} = \frac{1}{\sqrt{2N_1 N_2}} \mathbf{W}_1 \mathbf{w}_2, \quad (34a)$$

$$= \frac{1}{\sqrt{2N_1 N_2}} \begin{bmatrix} \mathbf{u}_{n_1, n_2}(q_1, q_2) & \mathbf{0}_{N_1 N_2 \times 1} \\ \mathbf{0}_{N_1 N_2 \times 1} & \mathbf{u}_{n_1, n_2}(q_1, q_2) \end{bmatrix} \begin{bmatrix} 1 \\ \varphi \end{bmatrix}. \quad (34b)$$

In (33) and (34), a single co-phasing value is applied over the entire bandwidth, referred to as Type-I wideband (WB). A higher-resolution alternative assigns a precoder to each group of subcarriers, called subband (SB). The Type-I SB selects co-phasing values φ_t (in $\mathbf{w}_{2,t}$) for each SB $t \in \{0, \dots, N_3 - 1\}$, where N_3 denotes the number of SBs [2].

2. Enhanced Type-II Codebook: Unlike Type-I, this codebook forms weighted combinations of $L \in \{2, 3, 4\}$ beams, yielding higher-resolution precoding that more closely approaches optimal eigen-beamforming. Due to dual polarization, the SD basis has a block-diagonal structure, that is

$$\mathbf{W}_1 = \begin{bmatrix} \mathbf{W}_{1p} & \mathbf{0}_{N_1 N_2 \times L} \\ \mathbf{0}_{N_1 N_2 \times L} & \mathbf{W}_{1p} \end{bmatrix} \in \mathbb{C}^{2N_1 N_2 \times 2L}, \quad (35a)$$

with

$$\mathbf{W}_{1p} = \begin{bmatrix} \mathbf{u}_{n_1^{(0)}, n_2^{(0)}}(q_1, q_2) & \dots & \mathbf{u}_{n_1^{(L-1)}, n_2^{(L-1)}}(q_1, q_2) \end{bmatrix}. \quad (35b)$$

The IDFT vectors in (35) are selected from the grid \mathcal{G} and use the same rotation indices (q_1, q_2) to ensure mutual orthogonality of the SD basis vectors.

The beams are combined using complex weights, referred to as beam combining coefficients (BCCs). A BCC is computed for each beam $i \in \{0, \dots, L - 1\}$, SB $t \in \{0, \dots, N_3 - 1\}$, and spatial layer $l \in \{1, \dots, \nu\}$, where ν denotes the transmission rank. This yields a layer-specific BCC matrix $\mathbf{W}_2^{(l)} \in \mathbb{C}^{2L \times N_3}$.

The eType-II codebook further applies frequency domain (FD) compression to exploit channel sparsity in the beam-delay domain, where each beam is associated with a limited number of delays. FD compression selects M_ν (rank-dependent) dominant delay vectors from an $N_3 \times N_3$ DFT matrix (without oversampling), whose columns are

$$\mathbf{y}_{n_3} = \begin{bmatrix} 1 e^{j \frac{2\pi n_3}{N_3}} & \dots & e^{j \frac{2\pi n_3 (N_3 - 1)}{N_3}} \end{bmatrix}^T, \quad n_3 \in \{0, \dots, N_3 - 1\}. \quad (36)$$

The resulting layer-specific FD basis $\mathbf{W}_f^{(l)} \in \mathbb{C}^{N_3 \times M_\nu}$ for layer l is applied to compress the BCC matrix as follows

$$\widetilde{\mathbf{W}}_2^{(l)} = \mathbf{W}_2^{(l)} \mathbf{W}_f^{(l)} \in \mathbb{C}^{2L \times M_\nu}, \quad (37)$$

To further reduce the feedback overhead, only the most significant $K^{NZ} < 2LM_\nu$ combining coefficients in $\widetilde{\mathbf{W}}_2^{(l)}$ are quantized, yielding the reported BCC matrix $\widetilde{\widetilde{\mathbf{W}}}_2^{(l)}$.

At the BS, the eType-II precoder associated with layer l is reconstructed as

$$\mathbf{W}^{(l)} = \mathbf{W}_1 \widetilde{\widetilde{\mathbf{W}}}_2^{(l)} \mathbf{W}_f^{(l)H} \in \mathbb{C}^{2N_1 N_2 \times N_3}, \quad (38)$$

where $(\cdot)^H$ is the conjugate transpose operator. It should be noted that normalization is applied to ensure that, for each SB t , the precoder $\mathbf{W}_t \in \mathbb{C}^{2N_1 N_2 \times \nu}$, satisfies $\mathbf{W}_t^H \mathbf{W}_t = \frac{1}{\nu} \mathbf{I}_\nu$, where \mathbf{I}_ν is the $\nu \times \nu$ identity matrix (Further details in [2]).

B. Precoder Selection Strategy

To select the best precoder from the 3GPP codebooks, we proceed as follows. First, the beam matrix is determined by selecting the rotation indices (q_1, q_2) and L IDFT vectors from the grid \mathcal{G} , with $L = 1$ for Type-I and $L > 1$ for eType-II. This selection can be based on the wideband channel covariance per polarization, \mathbf{R}_{11} and \mathbf{R}_{22} , defined as

$$\mathbf{R} = \begin{bmatrix} \mathbf{R}_{11} & \mathbf{R}_{12} \\ \mathbf{R}_{12}^H & \mathbf{R}_{22} \end{bmatrix} = \frac{1}{N_3} \sum_{t=0}^{N_3-1} \mathbf{H}_t^H \mathbf{H}_t, \quad (39)$$

where $\mathbf{H}_t \in \mathbb{C}^{N_R \times 2N_1 N_2}$ is the representative channel for SB t , obtained from CSI reference signals (CSI-RS)-based channel estimation. A detailed beam selection algorithm is given in [33, Algorithm 1].

1. Type-I Precoder: We describe the rank-1 case; higher ranks follow similarly. After beam selection, the co-phasing value $\varphi \in \{1, j, -1, -j\}$ is chosen to minimize interference. For each candidate φ , SINRs are computed using the precoder $\mathbf{w}(\varphi)$ and channel estimates $\mathbf{H}_{j,t}$ for each physical resource block (PRB) $j \in \{0, \dots, N_{SB} - 1\}$ within SB t , where N_{SB} is the number of PRBs per SB. Considering an LMMSE receiver, the SINR (for rank 1) is given as

$$\gamma_{j,t}(\varphi) = \frac{P}{\sigma_n^2} (\mathbf{w}(\varphi)^H \mathbf{H}_{j,t}^H \mathbf{H}_{j,t} \mathbf{w}(\varphi)), \quad (40)$$

where P is the transmit power and σ_n^2 is the noise variance. The SINRs are mapped to mutual information (MI) values for modulation order Q via $\mathcal{I}_Q(\cdot)$ and averaged over the bandwidth as follows

$$\frac{1}{N_3} \frac{1}{N_{SB}} \sum_{t=0}^{N_3-1} \sum_{j=0}^{N_{SB}-1} \mathcal{I}_Q(\gamma_{j,t}(\varphi)). \quad (41)$$

The co-phasing φ that maximizes (41) is selected.

2. Enhanced Type-II Precoder: Let the effective channel after SD compression be $\widetilde{\mathbf{H}}_t = \mathbf{H}_t \mathbf{W}_1 \in \mathbb{C}^{N_R \times 2L}$. The

combining coefficients are chosen to maximize the effective channel power under orthogonality constraints, i.e.

$$\mathbf{w}_{2,t}^{(l)} = \arg \max_{\mathbf{w}_2 \in \mathbb{C}^{2L} \setminus \{\mathbf{w}_{2,t}^{(l')}\}_{l'=1}^l} \mathbf{w}_2^H \overline{\mathbf{H}}_t^H \overline{\mathbf{H}}_t \mathbf{w}_2, \quad (42)$$

$$s.t. \quad \mathbf{w}_{2,t}^{(l)H} \mathbf{w}_{2,t}^{(l')} = 0, \quad \text{for } l' \neq l. \quad (43)$$

The optimal solution for SB t and layer l is the eigenvector associated with the l -th largest eigenvalue

$$\mathbf{w}_{2,t}^{(l)} = \text{eig}\left(\overline{\mathbf{H}}_t^H \overline{\mathbf{H}}_t\right)_l, \quad (44)$$

Phase normalization per-layer is then applied to $\mathbf{w}_{2,t}^{(l)}$ with respect to its largest-magnitude element, producing the BCC matrix $\widehat{\mathbf{W}}_2^{(l)}$. The FD basis for layer l is subsequently formed by sequentially selecting the M_ν dominant delays according to

$$n_3^{(f,l)} = \arg \max_{\substack{n_3 \in \{0, \dots, N_3-1\} \\ \{n_3^{(0,l)}, \dots, n_3^{(f-1,l)}\}}} \left(\widehat{\mathbf{W}}_2^{(l)} \mathbf{y}_{n_3}\right)^H \left(\widehat{\mathbf{W}}_2^{(l)} \mathbf{y}_{n_3}\right) \quad (45)$$

where \mathbf{y}_{n_3} is defined in (36). Finally, the BCC matrix is compressed according to (37), normalized, and quantized.

C. Physical-layer Abstraction

After PMI selection, the UE typically performs link adaptation to determine the transmission rank and the modulation and coding scheme (MCS), from which the CQI is derived. This process targets a given block error rate (BLER) based on an estimate of the effective SNR obtained from the CSI-RS channel estimate and given the PMI selected for each rank. In the RAN4 methodology, fixed MCS and rank values are assumed to facilitate comparison and cross-simulator alignment.

For performance evaluation, the SNR at the UE is estimated assuming an LMMSE receiver. The evaluation is conducted at the PRB level, i.e., based on $\mathbf{H}_{j,t}$ for PRB j within SB t . As we consider a single-user (SU)-MIMO scenario, it is reasonable to consider that the precoder selected at the UE-side, denoted $\mathbf{W}_t^{(\nu)}$, is used for downlink data transmission on ν spatial layers. The corresponding ground-truth precoded channel is given as $\mathbf{G}_{j,t}^{(\nu)} = \mathbf{H}_{j,t} \mathbf{W}_t^{(\nu)} \in \mathbb{C}^{N_R \times \nu}$. Demodulation reference signal (DMRS) channel estimation is applied at the UE to measure the precoded channel, yielding $\widehat{\mathbf{G}}_{j,t}^{(\nu)}$. Based on this estimate, the LMMSE equalizer is given by

$$\mathbf{F}_{j,t}^{(\nu)H} = \widehat{\mathbf{G}}_{j,t}^{(\nu)H} \left(\widehat{\mathbf{G}}_{j,t}^{(\nu)} \widehat{\mathbf{G}}_{j,t}^{(\nu)H} + \sigma_n^2/P \mathbf{I}_{N_R} \right)^{-1} \in \mathbb{C}^{\nu \times N_R}. \quad (46)$$

Using the filter in (46) and the ground-truth channel, the SINR at the output of the LMMSE receiver is estimated for each PRB. Let $\mathbf{g}_{j,t}^{(l,\nu)}$ denote the l -th column of $\mathbf{G}_{j,t}^{(\nu)}$ and $\mathbf{f}_{j,t}^{(l,\nu)H}$ the corresponding row of $\mathbf{F}_{j,t}^{(\nu)H}$. The SINR for PRB j within SB t is then given by

$$\gamma_{j,t}^{(l,\nu)} = \frac{|\mathbf{f}_{j,t}^{(l,\nu)H} \mathbf{g}_{j,t}^{(l,\nu)}|^2}{\mathbf{f}_{j,t}^{(l,\nu)H} \mathbf{C}_{j,t}^{(l,\nu)} \mathbf{f}_{j,t}^{(l,\nu)}} \quad (47a)$$

with the covariance of noise-plus-interference defined as

$$\mathbf{C}_{j,t}^{(l,\nu)} = \sum_{l' \neq l} \left(\mathbf{g}_{j,t}^{(l',\nu)} \mathbf{g}_{j,t}^{(l',\nu)H} \right) + \sigma_n^2/P \mathbf{I}_{N_R}. \quad (47b)$$

The resulting SINR values per PRB and spatial layer are mapped to a single effective value over the bandwidth for the rank ν and modulation Q , corresponding to the fixed MCS. This mapping is performed using the mutual information effective SINR mapping (MIESM) [34] as

$$\gamma_Q^{(\nu)} = \mathcal{I}_Q^{-1} \left(\frac{1}{\nu} \frac{1}{N_3} \frac{1}{N_{SB}} \sum_{l=1}^{\nu} \sum_{t=0}^{N_3-1} \sum_{j=0}^{N_{SB}-1} \mathcal{I}_Q(\gamma_{j,t}^{(l,\nu)}) \right) \quad (48)$$

where $\mathcal{I}_Q^{-1}(\cdot)$ is the inverse of $\mathcal{I}_Q(\cdot)$. The resulting effective SINR is compared with the SINR corresponding to the target BLER for the selected MCS. This reference SINR is obtained from BLER-versus-SNR lookup tables derived from LDPC decoding. The comparison yields an effective BLER, interpreted as the retransmission probability. With Chase combining, the SINR in dB after N_{rt} retransmissions is approximated as

$$\gamma_{j,t}^{(l,\nu)} = \gamma_{j,t}^{(l,\nu)} + 10 \log_{10}(N_{rt} + 1), \quad (49)$$

where $N_{rt} < N_{rt,\max}$, resulting in an updated BLER for each retransmission. The spectral efficiency is then computed as a function of the selected MCS (PDSCH tables in [3]), the number of retransmissions, and the transmission rank.

D. Simulation Results and Discussions

In this section, we evaluate the spectral efficiency of the Type-I (low-resolution) and eType-II (high-resolution) codebooks in a SU-MIMO scenario, as introduced in Sec. V-A. Performance is assessed using the PMI selection strategies in Sec. V-B together with the physical-layer abstraction framework in Sec. V-C.

Both ideal conditions and practical pilot-based channel estimation are considered. In the latter case, CSI-RS and DMRS pilots are generated and mapped onto the time-frequency grid according to the standard [35]. DMRS-based estimation averages consecutive least-squares (LS) estimates across PRBs within each frequency-domain bundle, assuming the channel is approximately constant over the bundle [36]. CSI-RS-based estimation uses a mismatched LMMSE approach assuming a flat power-delay profile for second-order statistics [37].

The primary objective is to identify configurations in which the performance gap between eType-II and Type-I is sufficiently large to distinguish their implementations. We focus on four parameters critical for realistic evaluation of 5G and beyond systems: (1) antenna panel configuration, (2) channel model, (3) channel estimation accuracy, and (4) angular spreads. A secondary objective is to demonstrate cross-simulator alignment for the considered channel model, supporting its suitability for defining performance requirements.

Monte Carlo simulations are conducted using the legacy TDLC300 model with medium-A correlation as defined

TABLE I
Simulation parameters

Antenna ports at BS	$(N_1, N_2) = (8, 2)$ for CDL model $(N_1, N_2) = (4, 2)$ for TDL model
Antenna ports at UE	$(N_1, N_2) = (1, 2)$
Antenna elements spacing	$d = 0.5\lambda_0$
Polarization slant angles at BS	$\zeta = +/ - 45^\circ$
Polarization slant angles at UE	$\zeta = 0/90^\circ$
Antenna radiation pattern at BS	Sector as in Table 7.3-1 of [1]
Antenna radiation pattern at UE	Isotropic
AAV	Direct port-to-element mapping
BS panel orientation	$(\alpha, \beta, \gamma) = (0^\circ, 10^\circ, 0^\circ)$
UE panel orientation	$(\alpha, \beta, \gamma) = (180^\circ, 0^\circ, 0^\circ)$
BS / UE height / BS-UE distance	25 m / 1.5 m / 100 m
Carrier frequency	3.5 GHz
Number of SB / PRBs per SB	$N_3 = 14 / N_{SB} = 8$
Bandwidth / Sub-carrier spacing	40 MHz / 30 kHz
UE speed / travel direction	3 km/h / $(\phi_v, \theta_v) = (65^\circ, 90^\circ)$
CSI/PMI reporting delay	7 ms
Modulation and coding scheme	MCS 7 from Table 5.1.3.1-2 of [1]
Rank/number of spatial layers	$\nu = 4$
Retransmission type	Chase with $N_{RT,max} = 4$
Type-II codebook parameters	paramCombination-r16=6
Energy per RE (EPRE) per antenna port (local constraint) [39]	only global power constraint considered
DMRS channel estimation	Type-1 with bundle size of 2 PRBs (baseline) or 4 (improved)
CSI-RS pilot positions	Row 17 of Table 7.4.1.5.3-1 of [35]
CSI-RS to PDSCH EPRE	1 (baseline) or 4 (improved)

in [6], as well as the rCDL-C model generated according to Algorithm 1, with an rms delay spread of 365 ns, following the tables in [17]. The study follows the RAN4 way forward (WF) for the SI on SCM for performance requirements [38]. Detailed simulation parameters are provided in Table I.

1. Antenna Panel Configuration: For CDL-based evaluations, we use $2N_1N_2 = 32$ transmit antenna ports. This large number of antennas provides degrees of freedom for beam selection, which can be exploited by eType-II, thereby increasing the potential performance gap between low- and high-resolution codebooks. For TDL-based evaluations, we use 16 transmit antenna ports since the standard does not specify this model with higher antenna counts.

2. Comparison of TDL and rCDL models under Ideal Channel Estimation: This section complements the observations in Sec. II-D regarding the limitations of the TDL model and shows that rCDL is suitable for evaluating CSI reporting requirements. Figs. 9 and 10 present the normalized spectral efficiency (w.r.t maximum MCS throughput) of Type-I and eType-II under the TDLC300 and rCDL-C models, respectively. For reference, two additional curves are included in all figures. The first

is a Type-I random PMI lower-bound (with uniformly drawn PMI). The second is an eigen-beamforming upper-bound, computed for each layer l and SB t as the l -th dominant eigenvector of the channel, i.e., $\text{eig}(\mathbf{H}_t^H \mathbf{H}_t)_l$, with equal power allocated across layers. This upper-bound is shown only when ideal channel estimation is considered, as it requires high estimation accuracy and is otherwise degraded.

Fig. 9 shows that Type-I and eType-II achieve nearly identical throughput. The medium-correlated TDL profile exhibits essentially a single dominant direction (cf. Fig. 2), which is well captured by the single-beam structure of Type-I. In addition, both codebooks operate significantly below the eigen-beamforming bound and relatively close to the random PMI lower-bound, indicating that they are not optimized for TDL-like channels. In contrast, Fig. 10 shows a clear performance gap under rCDL-C: the eType-II consistently achieves a gain of about 2 dB over Type-I under ideal channel estimation and operates close to the eigen-beamforming bound. This behavior is consistent with the eType-II design, in which linear combinations of multiple IDFT vectors approximate the channel eigenvectors. Moreover, under the rCDL model, both codebooks achieve a significant gain over the random PMI bound, as their design explicitly accounts for the spatial characteristics of MIMO propagation. Therefore, despite the simplifications introduced when deriving the reduced model from the legacy CDL model, rCDL continues to provide an accurate representation of MIMO propagation.

3. Effect of the Channel Estimation Accuracy: Fig. 11 shows the normalized spectral efficiency under the rCDL-C model with practical CSI-RS and DMRS channel estimation based on RAN4 settings. When comparing with Fig. 10, we observe that the performance gap between eType-II and Type-I decreases in the presence of estimation errors, particularly at low SNR. At 70% of the maximum throughput, eType-II provides about 1.5 dB gain, which drops below 0.5 dB at 50% throughput. This gap reduction occurs because high-resolution codebooks

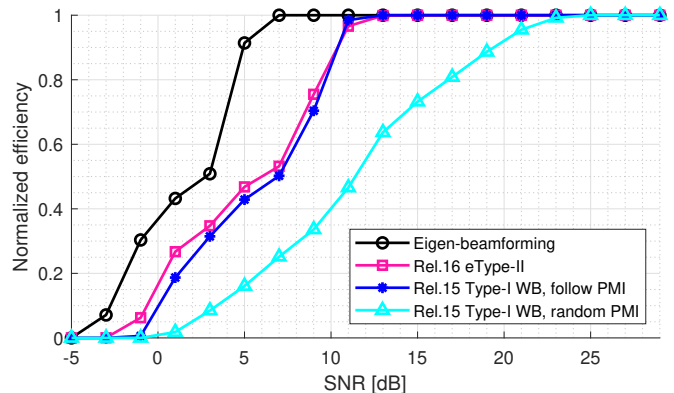


Fig. 9. Throughput performance of low- and high-resolution codebooks under TDLC300 with medium-A correlation and ideal channel estimation.

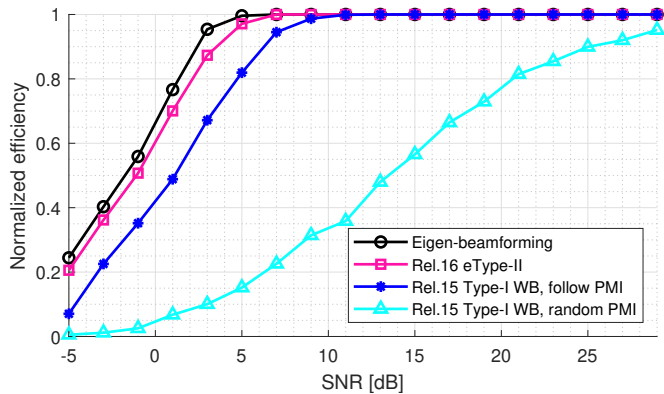


Fig. 10. Throughput performance of low- and high-resolution codebooks under rCDL-C with ideal channel estimation.

are more sensitive to estimation noise, whereas the coarser Type-I codebook is more robust by design. It should also be noted that the lower-bound is almost unchanged compared to the ideal case, as it is not affected by CSI-RS estimation errors, since there is no PMI selection.

The baseline estimation assumes equal CSI-RS and PDSCH EPRE. In practice, CSI-RS power can be boosted in the frequency domain by reallocating power from REs that are set to zero in the OFDM grid. In the following, considering pilots density and location, we apply a CSI-RS to PDSCH EPRE ratio of 4 to improve the estimation accuracy. Additionally, the DMRS bundle size is increased from 2 to 4 PRBs, thereby reducing estimation noise through averaging while assuming that the channel remains sufficiently stable across the bundle. Fig. 12 shows that under these improved conditions, eType-II consistently demonstrates a gain over Type-I even at negative SNR values, with the gap increasing up to 2 dB at 70% throughput, although it remains small at low SNR.

4. Effect of the Angular Spreads: Fig. 13 presents performance under improved channel estimation conditions while adopting the angular spreads defined in TR 38.901 for the RAN1 CDL-C model (scaled as

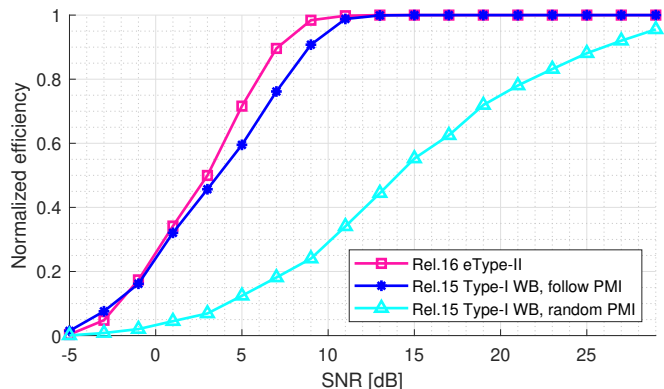


Fig. 11. Throughput performance of low- and high-resolution codebooks under rCDL-C with baseline CSI-RS and DMRS channel estimations.

described in Sec. III-C-1). We observe that Type-I performance degrades under RAN1 angular spreads compared to the tabulated rCDL-C model. This is mainly due to the smaller ASD in the rCDL-C, which limits the directional diversity. Larger spreads produce richer spatial structure that cannot be accurately represented by the low-resolution Type-I codebook, whereas eType-II remains capable of capturing this structure. Consequently, the performance gap increases, reaching 5 dB at 70% throughput. This confirms that spatial diversity, reflected in the angular spreads, is a key factor for differentiating the two schemes.

5. Cross-simulator Alignment: Simulations were also conducted using the antenna panel configuration from the RAN4 WF [38]. The study considers an 8Tx panel at the BS with direct antenna port-to-element mapping. The SNR values corresponding to 70% and 90% of the maximum throughput for 4-layer transmission reported by multiple companies in Table 7.1-3 of [17] exhibit a spread of less than 2.5 dB. This indicates a satisfactory degree of cross-simulator alignment for rCDL-C, supporting its suitability for defining MIMO performance requirements.

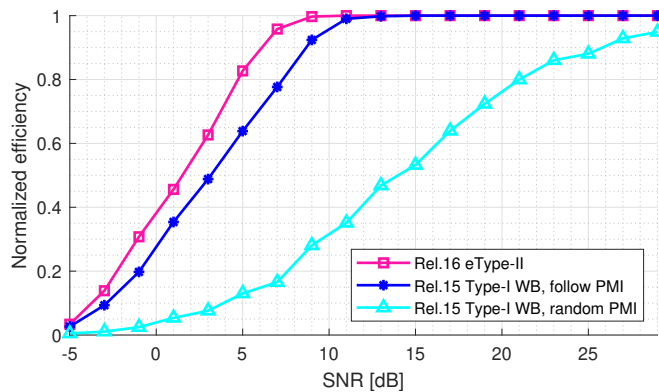


Fig. 12. Throughput performance of low- and high-resolution codebooks under rCDL-C with improved CSI-RS and DMRS channel estimations.

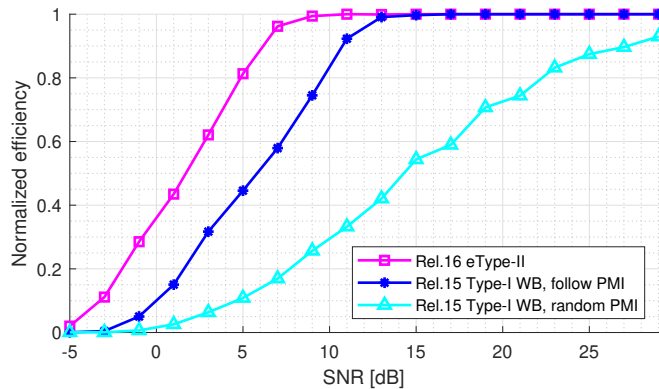


Fig. 13. Throughput performance of low- and high-resolution codebooks under rCDL-C with improved CSI-RS and DMRS channel estimation, and angular spreads of the TR38.901 CDL-C model.

VI. Conclusion

This paper investigated the rCDL model introduced in the RAN4 SI on channel modeling for performance requirements. We reviewed the legacy TDL model currently used by RAN4 and then described the derivation of the rCDL from the RAN1 CDL model specified in TR 38.901. The reduced model is designed to preserve the main propagation characteristics while lowering computational complexity and limiting randomness, making it suitable for repeatable RAN4 performance testing.

A comprehensive comparison between the rCDL and legacy TDL models was conducted using multiple approaches. First, spatial profile analysis showed that the rCDL captures multiple stable angular directions, whereas the TDL model is spatially agnostic. Second, measurements conducted in a typical MIMO deployment confirmed that CDL-based modeling more accurately reflects practical propagation conditions. Finally, as a case study, CSI reporting for SU-MIMO was evaluated. The results showed that the rCDL model enables clear discrimination between high- and low-resolution codebooks, whereas legacy TDL models do not. Hence, despite the simplifications made to the RAN1 CDL, the rCDL still yields meaningful MIMO performance assessment. We also identified parameters that require careful configuration to ensure valid evaluation of CSI feedback techniques. Future work includes extending the rCDL framework to a broader range of deployment scenarios, stabilizing the angular spread values from measurements, adapting the model for 6G systems, and considering MU-MIMO scenarios.

Appendix

Definition: Transformation between the GCS and LCS
Let the coordinates of a point be $\hat{\rho} = (x, y, z)$ in the GCS and $\hat{\rho}' = (x', y', z')$ in the LCS', these two sets of coordinates are related via the composite rotation matrix \mathbf{R} as

$$\hat{\rho} = \mathbf{R} \hat{\rho}' \text{ and } \hat{\rho}' = \mathbf{R}^{-1} \hat{\rho}, \quad (50)$$

where $\mathbf{R}^{-1} = \mathbf{R}^T$ (as \mathbf{R} is orthogonal) is the reverse transformation. This rotation results from the product of the three elementary rotations described in III-A-2, that is

$$\mathbf{R} = \mathbf{R}_z(\alpha)\mathbf{R}_y(\beta)\mathbf{R}_x(\gamma) = \begin{bmatrix} \cos \alpha & -\sin \alpha & 0 \\ \sin \alpha & \cos \alpha & 0 \\ 0 & 0 & 1 \end{bmatrix} \begin{bmatrix} \cos \beta & 0 & \sin \beta \\ 0 & 1 & 0 \\ -\sin \beta & 0 & \cos \beta \end{bmatrix} \begin{bmatrix} 1 & 0 & 0 \\ 0 & \cos \gamma & -\sin \gamma \\ 0 & \sin \gamma & \cos \gamma \end{bmatrix} \quad (51)$$

The direct transformation between the GCS and LCS'' can be operated by considering $\mathbf{R}_x(\gamma + \zeta)$ instead of $\mathbf{R}_x(\gamma)$ in (51).

1. Angles transformation (GCS \rightarrow LCS'') The fields are defined in (19) based on the clusters' angles in LCS''.

Transformation of the angles to LCS'' is operated using the inverse rotation matrix \mathbf{R}^{-1} , which yields

$$\theta'' = \arccos [\cos \beta \cos (\gamma + \zeta) \cos \theta + \sin \theta (\sin \beta \cos (\gamma + \zeta) \cos (\phi - \alpha) - \sin (\gamma + \zeta) \sin (\phi - \alpha))] \quad (52a)$$

$$\phi'' = \arg \{ \cos \beta \sin \theta \cos (\phi - \alpha) - \sin \beta \cos \theta + j (\cos \beta \sin (\gamma + \zeta) \cos \theta + \sin \theta [\sin \beta \sin (\gamma + \zeta) \cos (\phi - \alpha) + \cos (\gamma + \zeta) \sin (\phi - \alpha)]) \} \quad (52b)$$

Proof. Consider a point (x, y, z) on the unit sphere defined by the spherical coordinates (ρ, θ, ϕ) (with $\rho = 1$). The cartesian representation of that point is given by

$$\hat{\rho} = \begin{bmatrix} x \\ y \\ z \end{bmatrix} = \begin{bmatrix} \sin \theta \cos \phi \\ \sin \theta \sin \phi \\ \cos \theta \end{bmatrix} \quad (53)$$

Given (53) and considering that a point represented by $\hat{\rho}$ in the GCS corresponds to $\mathbf{R}^{-1}\hat{\rho}$ in the LCS'', we can show that

$$\theta'' = \arccos ([0 \ 0 \ 1] \mathbf{R}^{-1}\hat{\rho}), \quad (54a)$$

$$\phi'' = \arg ([1 \ j \ 0] \mathbf{R}^{-1}\hat{\rho}), \quad (54b)$$

which yields formulas in (52).

2. Fields transformation (LCS'' \rightarrow GCS) Double-primed fields as defined in (19) are transformed to GCS as follows

$$\mathbf{F}(\theta, \phi) = \begin{bmatrix} \hat{\theta}^T \mathbf{R} \hat{\theta}'' & \hat{\theta}^T \mathbf{R} \hat{\phi}'' \\ \hat{\phi}^T \mathbf{R} \hat{\theta}'' & \hat{\phi}^T \mathbf{R} \hat{\phi}'' \end{bmatrix} \mathbf{F}''(\theta'', \phi'') \quad (55)$$

It can be shown that this is equivalent to an angular displacement of ψ between the two pairs of unit vectors, i.e.,

$$\begin{bmatrix} \hat{\theta}^T \mathbf{R} \hat{\theta}'' & \hat{\theta}^T \mathbf{R} \hat{\phi}'' \\ \hat{\phi}^T \mathbf{R} \hat{\theta}'' & \hat{\phi}^T \mathbf{R} \hat{\phi}'' \end{bmatrix} = \begin{bmatrix} \cos \psi & -\sin (\psi) \\ \sin (\psi) & \cos \psi \end{bmatrix} \quad (56)$$

with $\psi = \arg \{ \hat{\theta}^T \mathbf{R} \hat{\theta}'' + j \hat{\phi}^T \mathbf{R} \hat{\theta}'' \}$. The angle can be expressed as function of the rotation angles $(\alpha, \beta, \gamma + \zeta)$ and the spherical position (θ, ϕ) as

$$\psi = \arg \{ \sin (\gamma + \zeta) \cos \theta \sin (\phi - \alpha) + \cos (\gamma + \zeta) (\cos \beta \sin \theta - \sin \beta \cos \theta \cos (\phi - \alpha)) + j [\sin (\gamma + \zeta) \cos (\phi - \alpha) + \sin \beta \cos (\gamma + \zeta) \sin (\phi - \alpha)] \} \quad (57)$$

The operations described above to calculate the field in the GCS are referred to as polarization Model-1 in the standard. An alternative model (Model-2) is also defined in [1]. The latter considers that the radiation power is split into the co-polar and cross-polar components as

$$\mathbf{F}'(\theta', \phi') = \begin{bmatrix} F'_{\theta'}(\theta', \phi') \\ F'_{\phi'}(\theta', \phi') \end{bmatrix} = \sqrt{A'(\theta', \phi')} \begin{bmatrix} \cos \zeta \\ \sin \zeta \end{bmatrix} \quad (58)$$

where $A'(\theta', \phi') = A''(\theta'', \phi'')$ with $\theta'' = \theta'$ and $\phi'' = \phi'$. The fields are then transformed from the LCS' to the GCS based on (55) with ψ defined as in (57) by replacing $(\gamma + \zeta)$ by γ , as polarization is already considered.

References

- [1] 3GPP, “5G; Study on channel model for frequencies from 0.5 to 100 GHz,” 3rd Generation Partnership Project (3GPP), Technical Report (TR) 38.901, October 2025, version 19.1.0.
- [2] X. Fu, D. Le Ruyet, R. Visoz, V. Ramireddy, M. Grossmann, M. Landmann, and W. Quiroga, “A tutorial on downlink precoder selection strategies for 3GPP MIMO codebooks,” *IEEE Access*, vol. 11, pp. 138 897–138 922, 2023.
- [3] 3GPP, “Physical layer procedures for data in 5G-NR (Release 18),” 3rd Generation Partnership Project (3GPP), Technical Specification (TS) 38.214, October 2025, version 19.1.0.
- [4] RP-241610, “New SID: study on spatial channel model for demodulation performance requirements,” Nokia, BT Plc et al., 3GPP TSG-RAN Meeting No. 104, June 2024, agenda item: 9.1.4, Document for: Approval.
- [5] P. Almers, E. Bonek, A. Burr, N. Czink, M. Debbah, V. Degli-Esposti, H. Hofstetter, P. Kyösti, D. Laurenson, G. Matz et al., “Survey of channel and radio propagation models for wireless mimo systems,” *EURASIP Journal on Wireless Communications and Networking*, vol. 2007, no. 1, p. 019070, 2007.
- [6] 3GPP, “5G; NR; User equipment (UE) radio transmission and reception; Part 4: performance requirements,” 3rd Generation Partnership Project (3GPP), Technical Specification (TS) 38.101-4, October 2025, version 19.0.0.
- [7] Y. R. Zheng and C. Xiao, “Simulation models with correct statistical properties for rayleigh fading channels,” *IEEE Transactions on Communications*, vol. 51, no. 6, pp. 920–928, 2003.
- [8] L. Schumacher, K. Pedersen, and P. Mogensen, “From antenna spacings to theoretical capacities - guidelines for simulating MIMO systems,” in *The 13th IEEE International Symposium on Personal, Indoor and Mobile Radio Communications*, vol. 2, 2002, pp. 587–592 vol.2.
- [9] Z. Yun and M. F. Iskander, “Ray tracing for radio propagation modeling: Principles and applications,” *IEEE Access*, vol. 3, pp. 1089–1100, 2015.
- [10] L. Correia, “COST action 273: Towards mobile broadband multimedia networks,” Final Report, 2006.
- [11] L. Liu, C. Oestges, J. Poutanen, K. Haneda, P. Vainikainen, F. Quitin, F. Tufvesson, and P. D. Doncker, “The cost 2100 mimo channel model,” *IEEE Wireless Communications*, vol. 19, no. 6, pp. 92–99, 2012.
- [12] 3GPP, “UMTS, spatial channel model for multiple input multiple output (MIMO) simulations,” 3rd Generation Partnership Project (3GPP), Technical Report (TR) 25.996, Sep. 2003, version 6.1.0.
- [13] D. S. Baum, J. Hansen, J. Salo, G. Del Galdo, M. Milojevic, and P. Kyösti, “An interim channel model for beyond-3G systems: extending the 3GPP spatial channel model (SCM),” in *2005 IEEE 61st Vehicular Technology Conference*, vol. 5. IEEE, 2005, pp. 3132–3136.
- [14] F. Ademaj, M. Taranetz, and M. Rupp, “3GPP 3D MIMO channel model: a holistic implementation guideline for open source simulation tools,” *EURASIP Journal on Wireless Communications and Networking*, vol. 2016, pp. 1–14, 2016.
- [15] D. Baum, H. El-Sallabi, T. Jämsä, J. Meinilä, P. Kyösti, X. Zhao, D. Laselva, J. Nuutinen, L. Hentila, P. Vainikainen, J. Kivinen, L. Vuokko, P. Zetterberg, M. Bengtsson, K. Yu, N. Jalden, T. Rautiainen, K. Kalliola, M. Milojevic, and J. Hansen, “Final report on link level and system level channel models,” IST-2003-507581 WINNER D5.4 V.1.4, 01 2005.
- [16] P. Kyösti, J. Meinilä, L. Hentila, X. Zhao, T. Jämsä, M. Narandzic, M. Milojević, A. Hong, J. Ylitalo, V.-M. Holappa, M. Alatossava, R. Bultitude, Y. Jong, and T. Rautiainen, “WINNER II channel models,” IST-4-027756 WINNER II D1.1.2 V1.2, 02 2008.
- [17] 3GPP, “Study on spatial channel model for demodulation performance requirements for NR,” 3rd Generation Partnership Project (3GPP), Technical Report (TR) 38.753, October 2025, version 19.0.0.
- [18] RP-252956, “New SID: Study on spatial channel model for demodulation performance requirements for NR: Phase 2,” Apple, 3GPP TSG RAN Meeting No. 109, Sep. 2025, agenda item: 9.3.4.3, Document for: Approval.
- [19] R. H. Clarke, “A statistical theory of mobile-radio reception,” *The Bell System Technical Journal*, vol. 47, no. 6, pp. 957–1000, 1968.
- [20] W. C. Jakes and D. C. Cox, *Microwave Mobile Communications*. Wiley-IEEE Press, 1994.
- [21] R4-071444, “Text proposal to 36.803 for MIMO correlation matrices,” Motorola, Agilent Technologies, Ericsson, Nokia, 3GPP TSG-RAN WG4 Meeting No. 44, Aug. 2007, agenda item: 8.3.2, Document for: Approval.
- [22] R4-071317, “Discussion on per channel versus per path correlation,” Agilent Technologies, 3GPP TSG-RAN WG4 Meeting No. 44, Aug. 2007, agenda item: 8.3.2, Document for: Discussion.
- [23] R4-072223, “TP for 36.803 for MIMO correlation matrices for LTE,” Motorola, Ericsson, Nokia, NEC, NXP, InterDigital, Agilent, 3GPP TSG-RAN WG4 Meeting No. 45, Nov. 2007, agenda item: 6.2.2.4, Document for: Approval.
- [24] R4-080127, “E-UTRA correlation matrixes for 4x2 and 4x4 antennas,” Ericsson, 3GPP TSG-RAN WG4 Meeting No. 46, Feb. 2008, agenda item: 6.1.2.4, Document for: Approval.
- [25] R4-1708533, “Discussion on SI for 8Rx,” Huawei, HiSilicon, 3GPP TSG RAN WG4 Meeting No. 84, Aug. 2017, agenda item: 10.1, Document for: Discussion.
- [26] G. Durgin and T. Rappaport, “Effects of multipath angular spread on the spatial cross-correlation of received voltage envelopes,” in *1999 IEEE 49th Vehicular Technology Conference (Cat. No.99CH36363)*, vol. 2, 1999, pp. 996–1000 vol.2.
- [27] H. L. Van Trees, *Optimum array processing: Part IV of detection, estimation, and modulation theory*. John Wiley & Sons, 2002.
- [28] 3GPP, “High power for NR TDD intra-band carrier aggregation in frequency range FR1,” 3rd Generation Partnership Project (3GPP), Technical Report (TR) 38.897, June 2024, version 18.0.0.
- [29] 3GPP, “Study on radiated metrics and test methodology for the verification of multi-antenna reception performance of NR user equipment (UE),” 3rd Generation Partnership Project (3GPP), Technical Report (TR) 38.827, September 2022, version 16.8.0.
- [30] R4-2402277, “Discussion on 8rx general demodulation aspects and spatial channel models,” Nokia, BT Plc, 3GPP TSG-RAN WG4 Meeting No. 110, Feb. 2024, agenda item: 8.1.3.1.1, Document for: Information.
- [31] R4-2419338, “Further observations on the properties of mimo channels in typical deployments,” BT, Ericsson, 3GPP TSG-RAN WG4 Meeting No. 113, Nov. 2024, agenda item: 7.14.1, Document for: Information.
- [32] A. Tukmanov, J. Weng, and R. Husbands, “Polarization and correlation in mimo channels,” in *WSA & SCC 2023; 26th International ITG Workshop on Smart Antennas and 13th Conference on Systems, Communications, and Coding*, 2023.
- [33] L. Berrah, R. Visoz, and D. Le Ruyet, “Channel prediction strategy for 3GPP Release 18 enhanced Type-II Doppler codebook,” in *2024 20th International Conference on Wireless and Mobile Computing, Networking and Communications (WiMob)*, 2024, pp. 489–495.
- [34] A. M. Cipriano, R. Visoz, and T. Salzer, “Calibration issues of phy layer abstractions for wireless broadband systems,” in *2008 IEEE 68th Vehicular Technology Conference*. IEEE, 2008, pp. 1–5.
- [35] 3GPP, “5G; NR; Physical channels and modulation,” 3rd Generation Partnership Project (3GPP), Technical Specification (TS) 38.211, Apr. 2025, version 18.6.0.
- [36] E. Dahlman, S. Parkvall, and J. Sköld, “Chapter 9 - transport-channel processing,” in *5G/5G-Advanced*, 3rd ed. Academic Press, 2024, pp. 189–218. [Online]. Available: <https://www.sciencedirect.com/science/article/pii/B9780443131738000104>
- [37] L. Berrah, R. Visoz, and D. Le Ruyet, “Noise-robust CSI prediction for 3GPP release 18 enhanced Type-II Doppler codebook,” in *2025 IEEE 36th International Symposium on Personal, Indoor and Mobile Radio Communications (PIMRC)*, 2025.
- [38] R4-2508624, “Way forward for [115][321] NR_SCM,” Nokia, 3GPP TSG-RAN WG4 Meeting No. 115, May 2025, agenda item: 7.16.1, Document for: Information.
- [39] R1-2410246, “CSI acquisition improvement for Type-II codebook,” Orange, ZTE, BT, 3GPP TSG RAN WG1 Meeting No. 119, Nov. 2024, agenda item: 9.12 TEI, Document for: Discussion and Decision.